Chapter 2
Fundamental Theory for Chemical Dissolution-Front Instability Problems in Fluid-Saturated Porous Media

When fresh pore-fluid enters a solute-saturated porous medium, where the concentration of the solute (i.e. aqueous mineral) reaches its equilibrium concentration, the concentration of the aqueous mineral is diluted so that the solid part of the solute (i.e. solid mineral) is dissolved to maintain the equilibrium state of the solution. This chemical dissolution process can result in the propagation of a dissolution front within the fluid-saturated porous medium. Due to the dissolution of the solid mineral, the porosity of the porous medium is increased behind the dissolution front. Since a change in porosity can cause a remarkable change in permeability, there is a feedback effect of the porosity change on the pore-fluid flow, according to Darcy's law. Because pore-fluid flow plays an important role in the process of reactive chemical-species transport, a change in pore-fluid flow can cause a considerable change in the chemical-species concentration within the porous medium (Steefel and Lasage 1990, 1994; Yeh and Tripathi 1991; Raffensperger and Garven 1995; Schafer et al. 1998a, b; Xu et al. 1999, 2004; Ormond and Ortoleva 2000; Chen and Liu 2002; Zhao et al. 2005, 2006a). This means that the problem associated with the propagation of a dissolution front is a fully coupled nonlinear problem between porosity, pore-fluid pressure and reactive chemical-species transport within the fluid-saturated porous medium. If the fresh pore-fluid flow is slow, the feedback effect of the porosity change is weak so that the dissolution front is stable. However, if the fresh pore-fluid flow is fast enough, the feedback effect of the porosity change becomes strong so that the dissolution front becomes unstable. In this case, a new morphology (i.e. dissipative structure) of the dissolution front can emerge due to the self-organization of this coupled nonlinear system. This leads to an important scientific problem, known as the chemical dissolution front instability problem (Zhao et al. 2008a, b), which is closely associated with mineral dissolution in a fluid-saturated porous medium.

C. Zhao, *Physical and Chemical Dissolution Front Instability in Porous Media*, Lecture Notes in Earth System Sciences,
DOI: 10.1007/978-3-319-08461-9_2

This kind of chemical dissolution-front instability problem exists ubiquitously in many scientific and engineering fields. For example, in geo-environmental engineering, the rehabilitation of contaminated sites using fresh water to wash the sites involves the propagation problem of the removed contaminant material front in a water-saturated porous medium. In mineral mining engineering, the extraction of minerals in the deep Earth using the in-situ leaching technique may result in the propagation problem of the dissolved mineral front in a fluid-saturated porous medium. In the petroleum industry, the secondary recovery of oil by acidifying the oil field to uniformly increase porosity and hence the yield of oil is associated with the propagation of the acid-dissolved material front in porous rocks. More importantly, due to the ever-increasing demand for mineral resources and the likelihood of the exhaust of the existing ore deposits, it is imperative to develop advanced techniques to explore for new ore deposits. Towards this goal, there is a definite need to understand the important physical and chemical processes that control ore body formation and mineralization in the deep Earth (Raffensperger and Garven 1995; Zhao et al. 1998, 1999, 2001a, b, 2003, 2006b, 2007, 2008c; Gow et al. 2002; Schaubs and Zhao 2002). According to modern mineralization theory, ore body formation and mineralization is mainly controlled by pore-fluid flow focusing and the equilibrium concentration gradient of the concerned minerals (Phillips 1991; Zhao et al. 1998). Since the chemical dissolution front can create porosity and therefore can locally enhance the pore-fluid flow, it becomes a potentially powerful mechanism to control ore body formation and mineralization in the deep Earth.

Although analytical solutions can be obtained for some reactive transport problems with simple geometry, it is very difficult, if not impossible, to predict analytically the complicated morphological evolution of a chemical dissolution front in the case of the chemical dissolution system becoming supercritical. As an alternative, numerical methods are suitable to overcome this difficulty. Since numerical methods are approximate solution methods, they must be validated before they are used to solve any new type of scientific and engineering problem. For this reason, it is necessary to derive the analytical solution for the propagation of a planar dissolution front within a benchmark problem, the geometry of which can be accurately simulated using numerical methods such as the finite element method (Zienkiewicz 1977; Lewis and Schrefler 1998) and the finite difference method. This makes it possible to compare the numerical solution obtained from the benchmark problem with the derived analytical solution so that the proposed numerical procedure can be verified for simulating the chemical dissolution-front propagation problem in a fluid-saturated porous medium.

2.1 Mathematical Theory for Simulating Chemical Dissolution-Front Instability Problems in Fluid-Saturated Porous Media

2.1.1 A General Case of Reactive Multi-Chemical-Species Transport with Consideration of Porosity/Permeability Feedback

For a pore-fluid-saturated porous medium, Darcy's law can be used to describe pore-fluid flow and Fick's law can be used to describe mass transport phenomena respectively. If both the porosity change of the porous medium is caused by chemical dissolution of soluble solid minerals within the porous medium and the feedback effect of such a change on the variation of permeability and diffusivity are taken into account, the governing equations of the coupled nonlinear problem between porosity, pore-fluid flow and reactive multi-chemical-species transport in the pore-fluid-saturated porous medium can be expressed as follows:

$$\frac{\partial}{\partial t}(\rho_f \phi) + \nabla \cdot (\rho_f \phi \vec{u}_{linear}) = 0, \tag{2.1}$$

$$\vec{u} = \phi \vec{u}_{linear} = -\frac{k(\phi)}{\mu} \nabla p, \tag{2.2}$$

$$\frac{\partial}{\partial t}(\phi C_i) + \nabla \cdot (\phi C_i \vec{u}_{linear}) = \nabla \cdot [\phi D_i(\phi) \nabla C_i] + R_i \qquad (i = 1, 2, \ldots, N), \tag{2.3}$$

where $\vec{u}_{linear}$ is the averaged linear velocity vector within the pore space of the porous medium; $\vec{u}$ is the Darcy velocity vector within the porous medium; p and C_i are pressure and the concentration (moles/pore-fluid volume) of chemical species i; μ is the dynamic viscosity of the pore-fluid; ϕ is the porosity of the porous medium; $D_i(\phi)$ is the diffusivity of chemical species i; ρ_f is the density of the pore-fluid; N is the total number of all the chemical species to be considered in the system; R_i is the source/sink term of chemical species i due to the dissolution/precipitation of solid minerals within the system; $k(\phi)$ is the permeability of the porous medium.

It is noted that in Eqs. (2.1)–(2.3), the chemical species concentration, the fluid density and averaged linear velocity of the pore-fluid are defined in the pore space, while the source/sink term and the Darcy velocity of the pore fluid are defined in the whole medium space (Phillips 1991; Nield and Bejan 1992; Zhao et al. 1994).

Since the diffusivity of each chemical species is considered as a function of porosity, a common phenomenological relation can be used for describing this function (Bear 1972; Chadam et al. 1986; Zhao et al. 2008a).

$$D_i(\phi) = D_{0i}\phi^q \quad \left(\tfrac{3}{2} \le q \le \tfrac{5}{2}\right), \tag{2.4}$$

where D_{0i} is the diffusivity of chemical species i in pure water.

To consider the permeability change caused by a change in porosity, an equation is needed to express the relationship between permeability and porosity. In this regard, Detournay and Cheng (1993) stated that "The intrinsic permeability k is generally a function of the pore geometry. In particular, it is strongly dependent on porosity ϕ. According to the Carman-Kozeny law (Scheidegger 1974) which is based on the conceptual model of packing of spheres, a power law relation of $k \propto \phi^3 \Big/ (1-\phi)^2$ exists. Other models based on different pore geometry give similar power laws. Actual measurements on rocks, however, often yield power law relations with exponents for ϕ significantly larger than 3." In addition, Nield and Bejan (1992) stated that "The Carman-Kozeny law is widely used since it seems to be the best simple expression available." For these reasons, the Carman-Kozeny law will be used to calculate permeability k, for a given porosity ϕ.

$$k(\phi) = \frac{k_0(1-\phi_0)^2\phi^3}{\phi_0^3(1-\phi)^2}, \tag{2.5}$$

where ϕ_0 and k_0 are the initial reference porosity and permeability of the porous medium respectively.

The source/sink term of chemical species i due to the dissolution/precipitation of solid minerals within the system can be determined in the following manner (Chadam et al. 1986; Zhao et al. 2008a). At the particle level, it is assumed that the average volume of soluble grains is $\bar{V}_p$ and that the density of the soluble grains is D_p, which is defined as the number of the soluble gains per unit medium volume. If the volume fraction of insoluble gains is denoted by $\phi_{insoluble}$, then the final (i.e. maximum) porosity of the porous medium can be denoted by $\phi_f = 1 - \phi_{insoluble}$. In this case, the average volume of soluble grains can be expressed as follows:

$$\bar{V}_p = \frac{\phi_f - \phi}{D_p}. \tag{2.6}$$

At the particle level, the rate of grain-volume change due to chemical (precipitation) reaction is denoted by R_p, so that the rate of porosity change can be expressed as:

$$\frac{\partial\phi}{\partial t} = -D_p R_p. \tag{2.7}$$

Without loss of generality, it is assumed that the solid grains are dissolved according to the following formula:

$$Solid \Rightarrow \sum_{i=1}^{N} \chi_i X_i, \tag{2.8}$$

where χ_i is the stoichiometric coefficient of the ith chemical species; X_i represents chemical species i in the pore-fluid.

It is commonly assumed that the rate of grain-volume change due to a chemical reaction can be expressed as follows (Chadam et al. 1986):

$$R_p = \frac{1}{\rho_s} k_{chemical} A_p \left(\prod_{i=1}^{N} C_i^{\chi_i} - K_{eq} \right) \tag{2.9}$$

where A_p is the averaged surface area of soluble grains; $k_{chemical}$ and K_{eq} are the conventional rate constant and equilibrium constant of the chemical reaction respectively; ρ_s is the molar density (i.e. moles per volume) of the soluble grains.

The source/sink term of chemical species i due to the dissolution/precipitation of solid minerals within the system can be expressed as follows:

$$\begin{aligned} R_i &= -\chi_i k_{chemical} D_p A_p \left(\prod_{i=1}^{N} C_i^{\chi_i} - K_{eq} \right) \\ &= -\chi_i k_{chemical} \frac{A_p}{V_p} (\phi_f - \phi) \left(\prod_{i=1}^{N} C_i^{\chi_i} - K_{eq} \right). \end{aligned} \tag{2.10}$$

2.1.2 A Particular Case of Reactive Single-Chemical-Species Transport with Consideration of Porosity/Permeability Feedback

As a particular case, reactive transport involving single chemical-species dissolution in a fluid-saturated porous medium is first considered in this subsection. If the pore-fluid is incompressible, the governing equations of the reactive single-chemical-species transport problem in the fluid-saturated porous medium can be written as follows:

$$\frac{\partial \phi}{\partial t} - \nabla \cdot [\psi(\phi) \nabla p] = 0, \tag{2.11}$$

$$\frac{\partial}{\partial t}(\phi C) - \nabla \cdot [\phi D(\phi) \nabla C + C \psi(\phi) \nabla p] + \rho_s k_{Echemical} \frac{A_p}{V_p} (\phi_f - \phi)(C - C_{eq}) = 0, \tag{2.12}$$

$$\frac{\partial \phi}{\partial t} + k_{Echemical} \frac{A_p}{V_p} (\phi_f - \phi)(C - C_{eq}) = 0, \tag{2.13}$$

$$\psi(\phi) = \frac{k(\phi)}{\mu}, \tag{2.14}$$

$$k_{Echemical} = \frac{k_{chemical}}{\rho_s C_{eq}}, \tag{2.15}$$

where C and C_{eq} are the concentration and equilibrium concentration of the single chemical species; $k_{Echemical}$ is the comprehensive rate constant of the chemical reaction in the single chemical-species dissolution system. Other quantities in Eqs. (2.11)–(2.15) are of the same meanings as those defined in Eqs. (2.1)–(2.3) and (2.9).

In Eq. (2.15), $k_{chemical}$ is the conventional rate constant with the unit of mol/(m^2 · s), while ρ_s and C_{eq} have the unit of mol/m^3, $k_{Echemical}$ has the unit of m^4/(mol · s). Note that Eqs. (2.11) and (2.12) can be derived by substituting the linear average velocity into Eqs. (2.1) and (2.3) with consideration of a single-chemical species.

For this single-chemical-species system, it is very difficult, even if not impossible, to obtain a complete set of analytical solutions for the pore-fluid pressure, chemical species concentration and porosity within the fluid-saturated porous medium. However, in some special cases, it is possible to obtain analytical solutions for some variables involved in this single-chemical-species system. The first special case to be considered is a problem, in which a planar dissolution front propagates in the full space. Since the chemical dissolution front is of a planar shape, the problem, which is described by Eqs. (2.11)–(2.13) degenerates into a one-dimensional problem. For this particular case, analytical solutions can be obtained for both the propagation speed of the dissolution front and the downstream pressure gradient of the pore-fluid. The second special case to be considered is an asymptotic problem, in which the solid molar density greatly exceeds the equilibrium concentration of the chemical species, implying that the region of a considerable porosity change propagates very slowly within the fluid-saturated porous medium. In this particular case, it is possible to derive a complete set of analytical solutions for the pore-fluid pressure, chemical species concentration and porosity within the fluid-saturated porous medium. In addition, it is also possible to investigate the chemical dissolution-front instability in this particular case (Chadam et al. 1986; Zhao et al. 2008a).

2.1.2.1 The First Special Case

In this special case, the planar dissolution front is assumed to propagate in the positive x direction, so that all quantities are independent of the transverse coordinates y and z. For this reason, Eqs. (2.11)–(2.13) can be rewritten as follows:

$$\frac{\partial \phi}{\partial t} - \frac{\partial}{\partial x}\left[\psi(\phi)\frac{\partial p}{\partial x}\right] = 0, \tag{2.16}$$

$$\frac{\partial}{\partial t}(\phi C) - \frac{\partial}{\partial x}\left[\phi D(\phi)\frac{\partial C}{\partial x} + C\psi(\phi)\frac{\partial p}{\partial x}\right] + \rho_s k_{Echemical}\frac{A_p}{V_p}(\phi_f - \phi)(C - C_{eq}) = 0, \tag{2.17}$$

$$\frac{\partial \phi}{\partial t} + k_{Echemical}\frac{A_p}{V_p}(\phi_f - \phi)(C - C_{eq}) = 0. \tag{2.18}$$

If the chemical species is initially in an equilibrium state and fresh pore-fluid is injected at the location of x approaching negative infinity, then the boundary conditions of this special problem are expressed as

$$\lim_{x\to-\infty} C(x, t) = 0, \quad \lim_{x\to-\infty}\frac{\partial p(x, t)}{\partial x} = p'_{fx} \quad \text{(upstream boundary)}, \tag{2.19}$$

$$\lim_{x\to\infty} C(x, t) = C_{eq}, \quad \lim_{x\to\infty}\frac{\partial p(x, t)}{\partial x} = p'_{0x} \quad \text{(downstream boundary)}, \tag{2.20}$$

where p'_{fx} is the pore-fluid pressure gradient as x approaching negative infinity in the upstream of the pore-fluid flow; p'_{0x} is the unknown pore-fluid pressure gradient as x approaching positive infinity in the downstream of the pore-fluid flow. Since p'_{fx} drives the pore-fluid flow continuously along the positive x direction, it has a negative algebraic value (i.e. $p'_{fx} < 0$) in this analysis.

The initial condition for this theoretical problem is: $\phi(x, 0) = \phi_0$ expect at the negative infinity, where $\lim_{\bar{x}\to-\infty}\phi(x, 0) = \phi_f$. Note that ϕ_0 is the initial porosity of the porous medium.

If the propagation speed of the planar dissolution front is denoted by v_{front}, then it is possible to transform a moving boundary problem of the dissolution front (in an $x - t$ coordinate system) into a steady-state boundary problem of the dissolution front (in an $\xi - t$ coordinate system) using the following coordinate mapping:

$$\xi = x - v_{front}t. \tag{2.21}$$

It is necessary to relate partial derivatives with respect to ξ and t to those with respect to x and t (Turcotte and Schubert 1982).

$$\left(\frac{\partial}{\partial t}\right)_{\xi} = \left(\frac{\partial}{\partial t}\right)_{x} + \frac{\partial}{\partial x}\frac{\partial x}{\partial t} = \left(\frac{\partial}{\partial t}\right)_{x} + v_{front}\frac{\partial}{\partial x}, \tag{2.22}$$

$$\left(\frac{\partial}{\partial \xi}\right)_{t} = \left(\frac{\partial}{\partial x}\right)_{t}, \tag{2.23}$$

where derivatives are taken with x or t held constant as appropriate.

Since the transformed system in the $\xi - t$ coordinate system is in a steady state, the following equations can be derived from Eqs. (2.22) and (2.23).

$$\left(\frac{\partial}{\partial t}\right)_x = -v_{front}\frac{\partial}{\partial \xi}, \tag{2.24}$$

$$\left(\frac{\partial}{\partial \xi}\right)_t = \left(\frac{\partial}{\partial x}\right)_t. \tag{2.25}$$

Substituting Eqs. (2.24) and (2.25) into Eqs. (2.16)–(2.18) yields the following equations:

$$\frac{\partial}{\partial \xi}\left[\psi(\phi)\frac{\partial p}{\partial \xi} + v_{front}\phi\right] = 0, \tag{2.26}$$

$$\frac{\partial}{\partial \xi}\left[\phi D(\phi)\frac{\partial C}{\partial \xi} + C\psi(\phi)\frac{\partial p}{\partial \xi} + v_{front}(C - \rho_s)\right] = 0, \tag{2.27}$$

$$v_{front}\frac{\partial \phi}{\partial \xi} - k_{chemical}\frac{A_p}{V_p}(\phi_f - \phi)(C - C_{eq}) = 0. \tag{2.28}$$

Integrating Eqs. (2.26) and (2.27) from negative infinity to positive infinity and using the boundary conditions [i.e. Eqs. (2.19) and (2.20)] yields the following equations:

$$C_{eq}\psi(\phi_0)p'_{ox} + v_{front}\phi_0(C_{eq} - \rho_s) + v_{front}\phi_f\rho_s = 0, \tag{2.29}$$

$$\psi(\phi_0)p'_{ox} + v_{front}\phi_0 - \psi(\phi_f)p'_{fx} - v_{front}\phi_f = 0. \tag{2.30}$$

Solving Eqs. (2.29) and (2.30) simultaneously results in the following analytical solutions:

$$v_{front} = \frac{-\psi(\phi_0)p'_{0x}C_{eq}}{\phi_0 C_{eq} + (\phi_f - \phi_0)\rho_s} = \frac{u_{0x}C_{eq}}{\phi_0 C_{eq} + (\phi_f - \phi_0)\rho_s}, \tag{2.31}$$

$$p'_{0x} = \frac{\psi(\phi_f)[\phi_0 C_{eq} + (\phi_f - \phi_0)\rho_s]}{\psi(\phi_0)[\phi_0 C_{eq} + (\phi_f - \phi_0)(\rho_s + C_{eq})]}p'_{fx}, \tag{2.32}$$

where u_{0x} is the Darcy velocity in the far downstream of the flow as x approaches positive infinity. Using Darcy's law, u_{0x} can be expressed as

$$u_{0x} = \frac{\phi_0 C_{eq} + (\phi_f - \phi_0)\rho_s}{\phi_0 C_{eq} + (\phi_f - \phi_0)(\rho_s + C_{eq})}u_{fx}, \tag{2.33}$$

where u_{fx} is the Darcy velocity in the far upstream of the flow as x approaches negative infinity.

If the finite element method is used to solve this special problem, the accuracy of the finite element simulation can be conveniently evaluated by comparing the numerical solutions with the analytical ones for both the propagation speed of the planar dissolution front (i.e. v_{front}) and the Darcy velocity in the far downstream of the flow as x approaches positive infinity (i.e. u_{0x}).

2.1.2.2 The Second Special Case (Base Solutions for a Stable State)

Since the solid molar density greatly exceeds the equilibrium concentration of the chemical species, a small parameter, which is called the mineral dissolution ratio (Zhao et al. 2010), can be defined as follows:

$$\varepsilon = \frac{C_{eq}}{\rho_s} \ll 1. \tag{2.34}$$

To facilitate the theoretical analysis in the limit case of ε approaching zero, the following dimensionless parameters and variables can be defined for a two-dimensional problem.

$$\bar{x} = \frac{x}{L^*}, \quad \bar{y} = \frac{y}{L^*}, \tag{2.35}$$

$$\bar{C} = \frac{C}{C_{eq}}, \bar{p} = \frac{p}{p^*}, \quad \bar{\vec{u}} = \frac{\vec{u}}{u^*}, \tag{2.36}$$

$$\tau = \frac{t}{t^*}\varepsilon, \tag{2.37}$$

where τ is a slow dimensionless time to describe the slowness of the chemical dissolution that takes place in the system. Other characteristic parameters used in Eqs. (2.35)–(2.37) can be expressed as follows:

$$t^* = \frac{\bar{V}_p}{k_{Echemical} A_p C_{eq}}, \; L^* = \sqrt{\phi_f D(\phi_f) t^*}, \tag{2.38}$$

$$p^* = \frac{\phi_f D(\phi_f)}{\psi(\phi_f)}, \; u^* = \frac{\phi_f D(\phi_f)}{L^*}, \tag{2.39}$$

$$D^*(\phi) = \frac{\phi D(\phi)}{\phi_f D(\phi_f)}, \; \psi^*(\phi) = \frac{\psi(\phi)}{\psi(\phi_f)}. \tag{2.40}$$

Substituting Eqs. (2.35)–(2.40) into Eqs. (2.11)–(2.13) yields the following dimensionless equations:

$$\varepsilon\frac{\partial\phi}{\partial\tau}-\nabla\cdot[\psi^*(\phi)\nabla\bar{p}]=0, \tag{2.41}$$

$$\varepsilon\frac{\partial}{\partial\tau}(\phi\bar{C})-\nabla\cdot[D^*(\phi)\nabla\bar{C}+\bar{C}\psi^*(\phi)\nabla\bar{p}]-\frac{\partial\phi}{\partial\tau}=0, \tag{2.42}$$

$$\varepsilon\frac{\partial\phi}{\partial\tau}+(\phi_f-\phi)(\bar{C}-1)=0. \tag{2.43}$$

Similarly, the boundary conditions for this special case can be expressed in a dimensionless form as follows:

$$\lim_{\bar{x}\to\infty}\bar{C}(\bar{x},\,\tau)=1,\quad \lim_{\bar{x}\to\infty}\frac{\partial\bar{p}(\bar{x},\,\tau)}{\partial\bar{x}}=\bar{p}'_{0x}\quad\text{(downstream boundary)}, \tag{2.44}$$

$$\lim_{\bar{x}\to-\infty}\bar{C}(\bar{x},\,\tau)=0,\quad \lim_{\bar{x}\to-\infty}\frac{\partial\bar{p}(\bar{x},\,\tau)}{\partial\bar{x}}=\bar{p}'_{fx}\quad\text{(upstream boundary)}. \tag{2.45}$$

In this case, the initial condition for this theoretical problem is: $\phi(\bar{x},\,0)=\phi_0$ expect at the negative infinity, where $\lim_{\bar{x}\to-\infty}\phi(\bar{x},\,0)=\phi_f$.

It is noted that the propagation front due to chemical dissolution divides the problem domain into two regions, an upstream region and a downstream region, relative to the propagation front. Across this propagation front, the porosity undergoes a jump from its initial value into its final value. Thus, this dissolution-front propagation problem can be considered as a Stefan moving boundary problem (Chadam et al. 1986; Zhao et al. 2008a). In the limit case of ε approaching zero, the corresponding governing equations for the dimensionless variables of the problem in both the downstream region and the upstream region can be expressed below:

$$\bar{C}=1,\quad \nabla^2\bar{p}=0,\quad \phi=\phi_0\quad\text{(in the downstream region)}, \tag{2.46}$$

$$\nabla\cdot(\nabla\bar{C}+\bar{C}\nabla\bar{p})=0,\quad \nabla^2\bar{p}=0,\quad \phi=\phi_f\quad\text{(in the upstream region)}. \tag{2.47}$$

If the chemical dissolution front is denoted by $S(\bar{x},\,\tau)=0$, then the dimensionless pressure, chemical species concentration and mass fluxes of both the chemical species and the pore-fluid should be continuous on $S(\bar{x},\,\tau)=0$. This leads to the following interface conditions for this moving-front problem:

$$\lim_{S\to0^-}\bar{C}=\lim_{S\to0^+}\bar{C},\quad \lim_{S\to0^-}\bar{p}=\lim_{S\to0^+}\bar{p}, \tag{2.48}$$

$$\lim_{S\to0^-}\frac{\partial\bar{C}}{\partial n}=\bar{v}_{front}(\phi_f-\phi_0),\quad \lim_{S\to0^-}\frac{\partial\bar{p}}{\partial\bar{n}}=\frac{\psi(\phi_0)}{\psi(\phi_f)}\lim_{S\to0^+}\frac{\partial\bar{p}}{\partial\bar{n}}, \tag{2.49}$$

where $\bar{n} = n/L^*$; n is the normal vector of the propagating planar chemical dissolution-front; $\bar{v}_{front}$ is the dimensionless propagation speed of the planar chemical dissolution-front.

When the planar dissolution front is under stable conditions, the base solutions for this special problem can be derived from Eqs. (2.46) and (2.47) with the related boundary and interface conditions [i.e. Eqs. (2.44), (2.45), (2.48) and (2.49)]. The resulting base solutions are expressed as follows:

$$\bar{C}(\xi) = 1, \quad \bar{p}(\xi) = \bar{p}'_{0x}\xi + \bar{p}_{C1}, \quad \phi = \phi_0 \quad \text{(in the downstream region)}, \tag{2.50}$$

$$\bar{C}(\xi) = \exp(-\bar{p}'_{fx}\xi), \quad \bar{p}(\xi) = \bar{p}'_{fx}\xi + \bar{p}_{C2}, \quad \phi = \phi_f \quad \text{(in the upstream region)}, \tag{2.51}$$

where $\bar{p}_{C1}$ and $\bar{p}_{C2}$ are two constants to be determined. For example, $\bar{p}_{C1}$ can be determined by setting dimensionless pressure $\bar{p}(\xi)$ to be a constant at a prescribed location of the downstream region, while $\bar{p}_{C2}$ can be determined using the pressure continuity condition at the interface between the upstream and downstream regions. Other parameters are defined below:

$$\xi = \bar{x} - \bar{v}_{front}\tau, \quad \bar{p}'_{0x} = \frac{\psi(\phi_f)}{\psi(\phi_0)}\bar{p}'_{fx}, \quad \bar{v}_{front} = -\frac{\bar{p}'_{fx}}{\phi_f - \phi_0}. \tag{2.52}$$

Therefore, if the finite element method is used to solve the second special problem, the accuracy of the finite element simulation can be conveniently evaluated by comparing the numerical solutions with a complete set of analytical solutions including porosity, the location of the chemical dissolution front, the dimensionless chemical-species concentration and the dimensionless pore-fluid pressure.

2.1.2.3 The Second Special Case (Perturbation Solutions for an Unstable State)

When a reactive transport system represented by the above-mentioned second special problem is stable, the planar dissolution front remains planar, even though both small perturbations of the dissolution front and the feedback effect of porosity/permeability change are simultaneously considered in the analysis. However, when the reactive transport system is unstable, the planar dissolution front can change from a planar shape into a complicated one. The instability of the above-mentioned second special problem can be determined using a linear stability analysis (Chadam et al. 1986, 1988; Ortoleva et al. 1987; Zhao et al. 2008a). The main purpose of conducting such a linear stability analysis is to determine the critical condition under which the chemical dissolution front of the reactive transport system becomes unstable.

If a small time-dependent perturbation is added to the planar dissolution front, then the total solution of the system is equal to the summation of the base solution and the perturbed solution of the system.

$$S(\xi, \bar{y}, \tau) = \xi - \delta \exp(\bar{\omega}\tau)\cos(\bar{m}\bar{y}), \tag{2.53}$$

$$\bar{p}_{total}(\xi, \bar{y}, \tau) = \bar{p}(\xi, \tau) + \delta\,\hat{p}(\xi)\exp(\bar{\omega}\tau)\cos(\bar{m}\bar{y}), \tag{2.54}$$

$$\bar{C}_{total}(\xi, \bar{y}, \tau) = \bar{C}(\xi, \tau) + \delta\,\hat{C}(\xi)\exp(\bar{\omega}\tau)\cos(\bar{m}\bar{y}), \tag{2.55}$$

where $\bar{\omega}$ is the dimensionless growth rate of the perturbation; $\bar{m}$ is the dimensionless wavenumber of the perturbation; δ is the amplitude of the perturbation and $\delta \ll 1$ by the definition of a linear stability analysis.

Since $S(\xi, \bar{y}, \tau)$ is a function of coordinates $S(\xi, \bar{y}, \tau)$ and $\bar{y}$, the following derivatives exist mathematically:

$$\left(\frac{\partial}{\partial\xi}\right)_{\xi} = \frac{\partial S}{\partial\xi}\frac{\partial}{\partial S} = \left(\frac{\partial}{\partial\xi}\right)_{S}, \tag{2.56}$$

$$\left(\frac{\partial}{\partial\bar{y}}\right)_{\xi} = \frac{\partial S}{\partial\bar{y}}\frac{\partial}{\partial S} + \left(\frac{\partial}{\partial\bar{y}}\right)_{S} = \frac{\partial S}{\partial\bar{y}}\left(\frac{\partial}{\partial\xi}\right)_{S} + \left(\frac{\partial}{\partial\bar{y}}\right)_{S}, \tag{2.57}$$

$$\left(\frac{\partial^2}{\partial\xi^2}\right)_{\xi} = \left(\frac{\partial^2}{\partial\xi^2}\right)_{S}, \tag{2.58}$$

$$\left(\frac{\partial^2}{\partial\bar{y}^2}\right)_{\xi} = \frac{\partial^2 S}{\partial\bar{y}^2}\frac{\partial}{\partial\xi} + \left(\frac{\partial S}{\partial\bar{y}}\right)^2\frac{\partial^2}{\partial\xi^2} + 2\frac{\partial S}{\partial\bar{y}}\frac{\partial^2}{\partial\xi\partial\bar{y}} + \left(\frac{\partial^2}{\partial\bar{y}^2}\right)_{S}. \tag{2.59}$$

It is noted that the total solutions expressed in Eqs. (2.54) and (2.55) must satisfy the governing equations that are expressed in Eqs. (2.46) and (2.47). With consideration of Eq. (2.59), the first-order perturbation equations of this system can be expressed as

$$\hat{C} = 0, \quad \frac{\partial^2\hat{p}}{\partial\xi^2} - \bar{m}^2\hat{p} + \bar{m}^2\bar{p}'_{0x} = 0 \quad \text{(in the downstream region)}, \tag{2.60}$$

$$\frac{\partial^2\hat{C}}{\partial\xi^2} + \bar{p}'_{fx}\frac{\partial\hat{C}}{\partial\xi} - \bar{m}^2\hat{C} - \bar{m}^2\bar{p}'_{fx}\exp(-\bar{p}'_{fx}\xi) - \bar{p}'_{fx}\exp(-\bar{p}'_{fx}\xi)\frac{\partial\hat{p}}{\partial\xi} = 0,$$

$$\frac{\partial^2\hat{p}}{\partial\xi^2} - \bar{m}^2\hat{p} + \bar{m}^2\bar{p}'_{fx} = 0 \quad \text{(in the upstream region)}. \tag{2.61}$$

The corresponding boundary conditions of the first-order perturbation problem are:

$$\hat{C}(\xi) = 0, \quad \lim_{\xi \to \infty} \frac{\partial \hat{p}(\xi)}{\partial \xi} = 0 \quad \text{(downstream boundary)}, \tag{2.62}$$

$$\lim_{\xi \to -\infty} \hat{C}(\xi) = 0, \quad \lim_{\xi \to -\infty} \frac{\partial \hat{p}(\xi)}{\partial \xi} = 0 \quad \text{(upstream boundary)}. \tag{2.63}$$

Similarly, the interface conditions for this first-order perturbation problem can be expressed as follows:

$$\hat{C} = 0, \quad \lim_{S \to 0^-} \hat{p} = \lim_{S \to 0^+} \hat{p}, \tag{2.64}$$

$$\lim_{S \to 0^-} \frac{\partial \hat{C}}{\partial \bar{n}} = \bar{\omega}(\phi_f - \phi_0), \quad \lim_{S \to 0^-} \frac{\partial \hat{p}}{\partial \bar{n}} = \frac{\psi(\phi_0)}{\psi(\phi_f)} \lim_{S \to 0^+} \frac{\partial \hat{p}}{\partial \bar{n}}. \tag{2.65}$$

Solving Eqs. (2.60) and (2.61) with the boundary and interface conditions [i.e. Eqs. (2.62)–(2.65)] yields the following analytical results:

$$\hat{C} = 0, \quad \hat{p}(\xi) = \bar{p}'_{0x}\left[1 - \frac{1-\beta}{1+\beta}\exp(-|\bar{m}|\xi)\right] \quad \text{(in the downstream region)}, \tag{2.66}$$

$$\hat{C}(\xi) = -\bar{p}'_{fx}\left\{\exp(-\bar{p}'_{fx}\xi) - \frac{2}{1+\beta}\exp(\sigma\xi) + \frac{1-\beta}{1+\beta}\exp[(|\bar{m}| - \bar{p}'_{fx})\xi]\right\},$$

$$\hat{p}(\xi) = \bar{p}'_{fx}\left[1 + \frac{1-\beta}{1+\beta}\exp(|\bar{m}|\xi)\right] \quad \text{(in the upstream region)}, \tag{2.67}$$

where

$$\beta = \frac{\psi(\phi_0)}{\psi(\phi_f)} = \frac{k(\phi_0)}{k(\phi_f)}, \tag{2.68}$$

$$\sigma = \frac{\sqrt{(\bar{p}'_{fx})^2 + 4m^2} - \bar{p}'_{fx}}{2}. \tag{2.69}$$

Substituting Eq. (2.67) into Eq. (2.65) yields the following equation for the dimensionless growth rate of the small perturbation:

$$\bar{\omega}(\bar{m}) = \frac{-\bar{p}'_{fx}}{(1+\beta)(\phi_f - \phi_0)}\left[-\bar{p}'_{fx} - \sqrt{(\bar{p}'_{fx})^2 + 4\bar{m}^2} + (1-\beta)|\bar{m}|\right). \tag{2.70}$$

Equation (2.70) clearly indicates that the planar dissolution front of the reactive transport system, which is described by the above-mentioned second special problem, is stable to short wavelength (i.e. large dimensionless wavenumber $\bar{m}$) perturbations but it is unstable to long wavelength (i.e. small dimensionless wavenumber $\bar{m}$) perturbations.

Letting $\bar{\omega}(\bar{m}) = 0$ yields the following critical condition, under which the reactive transport system can become unstable.

$$\bar{p}'_{fx}\Big|_{critical} = -\frac{(3-\beta)(1+\beta)}{2(1-\beta)}, \tag{2.71}$$

where $\bar{p}'_{fx}\Big|_{critical}$ is the critical value of the generalized dimensionless pressure gradient in the far upstream direction as x approaching negative infinity (Zhao et al. 2008a). Since $\bar{p}'_{fx}\Big|_{critical}$ is usually of a negative value, the following critical Zhao number is defined to judge the instability of the reactive transport system:

$$Zh_{critical} = -\bar{p}'_{fx}\Big|_{critical} = \frac{(3-\beta)(1+\beta)}{2(1-\beta)}. \tag{2.72}$$

Thus, the Zhao number of the reactive transport system can be defined as follows:

$$Zh = -\bar{p}'_{fx} = -\frac{p'_{fx}L^*}{p^*} = -\frac{k(\phi_f)L^*p'_{fx}}{\phi_f \mu D(\phi_f)} = \frac{v_{flow}}{\sqrt{\phi_f D(\phi_f)}}\sqrt{\frac{\bar{V}_p}{k_{Echemical}A_p C_{eq}}}. \tag{2.73}$$

where v_{flow} is the Darcy velocity of the injected pore-fluid flow; ϕ_f is the porosity when the dissolvable minerals are completely dissolved; $D(\phi_f)$ is the molecular diffusivity of the solute in the mineral completely-dissolved region; $\bar{V}_p$ is the average volume of soluble grains; A_p is the averaged surface area of soluble grains; C_{eq} is the equilibrium concentration of the dissolvable mineral; $k_{Echemical}$ is the equivalent rate constant of the chemical reaction in the single chemical-species dissolution system [as defined in Eq. (2.15)].

Using Eqs. (2.72) and (2.73), a criterion can be established to judge the instability of a chemical dissolution front associated with the particular chemical system in this investigation. If $Zh > Zh_{critical}$, then the chemical dissolution front of the reactive transport system becomes unstable, while if $Zh < Zh_{critical}$, then the chemical dissolution front of the reactive transport system is stable. The case of $Zh = Zh_{critical}$ represents a situation where the chemical dissolution front of the reactive transport system is neutrally unstable, implying that the introduced small perturbation can be maintained but it does not grow in the corresponding reactive transport system.

Clearly, Eq. (2.73) indicates that for the reactive chemical-species transport considered in this investigation, the dissolution-enhanced permeability destabilizes

the instability of the chemical dissolution front, while the dissolution-enhanced diffusivity stabilizes the instability of the chemical dissolution front. If the shape factor of soluble grains is represented by $\theta = \bar{V}_p/A_p$, then an increase in the shape factor of soluble grains can destabilize the instability of the chemical dissolution front, indicating that the instability likelihood of a porous medium comprised of irregular grains, is higher than that of a porous medium comprised of regular spherical grains. Similarly, an increase in either the equilibrium concentration of the chemical species or the chemical reaction constant of the dissolution reaction can cause the stabilization of the chemical dissolution front, for the reactive chemical-species transport considered in this investigation.

To understand the physical meanings of each term in the Zhao number, Eq. (2.73) can be rewritten in the following form:

$$Zh = F_{Advection} F_{Diffusion} F_{Chemical} F_{Shape}, \tag{2.74}$$

where $F_{Advection}$ is a term to represent the solute advection; $F_{Diffusion}$ is a term to represent the solute diffusion/dispersion; $F_{Chemical}$ is a term to represent the chemical kinetics of the dissolution reaction; F_{Shape} is a term to represent the shape factor of the soluble mineral in the fluid-rock interaction system. These terms can be expressed as follows:

$$F_{Advection} = v_{flow}, \tag{2.75}$$

$$F_{Diffusion} = \frac{1}{\sqrt{\phi_f D(\phi_f)}}, \tag{2.76}$$

$$F_{Chemical} = \sqrt{\frac{1}{k_{chemical} C_{eq}}}, \tag{2.77}$$

$$F_{Shape} = \sqrt{\frac{\bar{V}_p}{A_p}}. \tag{2.78}$$

Equations (2.74)–(2.78) clearly indicate that the Zhao number is a dimensionless number that can be used to represent the geometrical, hydrodynamic, thermodynamic and chemical kinetic characteristics of a fluid-rock system in a comprehensive manner. This dimensionless number reveals the intimate interaction between solute advection, solution diffusion/dispersion, chemical kinetics and mineral geometry in a reactive transport system.

2.2 Computational Theory for Simulating the Morphological Evolution of a Chemical Dissolution Front

Although analytical solutions can be obtained for the above-mentioned special cases, it is very difficult, if not impossible, to predict analytically the complicated morphological evolution process of a planar dissolution front in the case of the chemical dissolution system becoming supercritical. As an alternative, numerical methods are suitable to overcome this difficulty. Since numerical methods are approximate solution methods, they must be validated before they are used to solve any new type of scientific and engineering problem. For this reason, the main purpose of this section is to propose a numerical procedure for simulating how a planar dissolution front evolves into a complicated morphological front. To verify the accuracy of the numerical solution, a benchmark problem is constructed from the theoretical analysis in Sect. 2.1.2.2. As a result, the numerical solution obtained from the benchmark problem can be compared with the corresponding analytical solution. After the proposed numerical procedure is verified, it will be used to simulate the complicated morphological evolution process of a planar dissolution front in the case of the chemical dissolution system becoming supercritical.

2.2.1 Formulation of the Segregated Algorithm for Simulating the Evolution of Chemical Dissolution Fronts

In this section, Eqs. (2.41)–(2.43) are solved using the proposed numerical procedure, which is a combination of both the finite element method and the finite difference method. The finite element method is used to discretize the geometrical shape of the problem domain, while the finite difference method is used to discretize the dimensionless time. Since the system described by these equations is highly nonlinear, the segregated algorithm, in which Eqs. (2.41)–(2.43) are solved separately in a sequential manner, is used to derive the formulation of the proposed numerical procedure.

For a given dimensionless time-step, $\tau + \Delta\tau$, the porosity can be denoted by $\phi_{\tau+\Delta\tau} = \phi_\tau + \Delta\phi_{\tau+\Delta\tau}$, where ϕ_τ is the porosity at the previous time-step and $\Delta\phi_{\tau+\Delta\tau}$ is the porosity increment at the current time-step. Using the backward difference scheme, Eq. (2.43) can be written as follows:

$$\left[\frac{\varepsilon}{\Delta\tau} + (1 - \bar{C}_{\tau+\Delta\tau})\right]\Delta\phi_{\tau+\Delta\tau} = (\phi_f - \phi_\tau)(1 - \bar{C}_{\tau+\Delta\tau}), \tag{2.79}$$

where $\bar{C}_{\tau+\Delta\tau}$ is the dimensionless concentration at the current time-step; $\Delta\tau$ is the dimensionless time increment at the current time-step.

Mathematically, there exist the following relationships in the finite difference sense:

$$\varepsilon\frac{\partial(\phi\bar{C})}{\partial\tau}=\varepsilon\frac{\Delta(\phi_{\tau+\Delta\tau}\bar{C}_{\tau+\Delta\tau})}{\Delta\tau}=\varepsilon\bar{C}_{\tau+\Delta\tau}\frac{\Delta\phi_{\tau+\Delta\tau}}{\Delta\tau}+\varepsilon\phi_{\tau+\Delta\tau}\frac{\Delta(\bar{C}_{\tau+\Delta\tau})}{\Delta\tau}, \tag{2.80}$$

$$\varepsilon\frac{\partial\phi}{\partial\tau}=\varepsilon\frac{\Delta(\phi_{\tau+\Delta\tau})}{\Delta\tau}=(1-\bar{C}_{\tau+\Delta\tau})(\phi_f-\phi_{\tau+\Delta\tau}), \tag{2.81}$$

$$\nabla\cdot[D^*(\phi)\nabla\bar{C}]=\nabla\cdot[D^*(\phi_{\tau+\Delta\tau})\nabla\bar{C}_{\tau+\Delta\tau}], \tag{2.82}$$

$$\begin{aligned}\nabla\cdot[\bar{C}\psi^*(\phi)\nabla\bar{p}]&=\bar{C}\nabla\cdot[\psi^*(\phi)\nabla\bar{p}]+\nabla\bar{p}\cdot[\psi^*(\phi)\nabla\bar{C}]\\&=\bar{C}_{\tau+\Delta\tau}\nabla\cdot[\psi^*(\phi_{\tau+\Delta\tau})\nabla\bar{p}_{\tau+\Delta\tau}]+\nabla\bar{p}_{\tau+\Delta\tau}\cdot[\psi^*(\phi_{\tau+\Delta\tau})\nabla\bar{C}_{\tau+\Delta\tau}].\end{aligned} \tag{2.83}$$

Substituting Eqs. (2.80)–(2.83) into Eq. (2.42) yields the following finite difference equation:

$$\begin{aligned}&\left[\frac{\varepsilon}{\Delta\tau}\phi_{\tau+\Delta\tau}+\frac{1}{\varepsilon}(\phi_f-\phi_{\tau+\Delta\tau})\right]\bar{C}_{\tau+\Delta\tau}-\nabla\cdot[D^*(\phi_{\tau+\Delta\tau})\nabla\bar{C}_{\tau+\Delta\tau}]\\&\quad-\nabla\bar{p}_{\tau+\Delta\tau}\cdot[\psi^*(\phi_{\tau+\Delta\tau})\nabla\bar{C}_{\tau+\Delta\tau}]=\frac{\varepsilon}{\Delta\tau}\phi_{\tau+\Delta\tau}\bar{C}_\tau+\frac{1}{\varepsilon}(\phi_f-\phi_{\tau+\Delta\tau}).\end{aligned} \tag{2.84}$$

Similarly, Eq. (2.41) can be rewritten in the following discretized form:

$$\nabla\cdot[\psi^*(\phi)\nabla\bar{p}]=\nabla\cdot[\psi^*(\phi_{\tau+\Delta\tau})\nabla\bar{p}_{\tau+\Delta\tau}]=(1-\bar{C}_{\tau+\Delta\tau})(\phi_f-\phi_{\tau+\Delta\tau}). \tag{2.85}$$

To derive the finite element equations of the problem, the corresponding finite difference equations can be summarized as follows:

$$\left[\frac{\varepsilon}{\Delta\tau}+(1-\bar{C}_{\tau+\Delta\tau})\right]\Delta\phi_{\tau+\Delta\tau}=(\phi_f-\phi_\tau)(1-\bar{C}_{\tau+\Delta\tau}), \tag{2.86}$$

$$\begin{aligned}&\left[\frac{\varepsilon}{\Delta\tau}\phi_{\tau+\Delta\tau}+\frac{1}{\varepsilon}(\phi_f-\phi_{\tau+\Delta\tau})\right]\bar{C}_{\tau+\Delta\tau}-\nabla\cdot[D^*(\phi_{\tau+\Delta\tau})\nabla\bar{C}_{\tau+\Delta\tau}]\\&\quad-\nabla\bar{p}_{\tau+\Delta\tau}\cdot[\psi^*(\phi_{\tau+\Delta\tau})\nabla\bar{C}_{\tau+\Delta\tau}]=\frac{\varepsilon}{\Delta\tau}\phi_{\tau+\Delta\tau}\bar{C}_\tau+\frac{1}{\varepsilon}(\phi_f-\phi_{\tau+\Delta\tau}),\end{aligned} \tag{2.87}$$

$$\nabla\cdot[\psi^*(\phi)\nabla\bar{p}]=\nabla\cdot[\psi^*(\phi_{\tau+\Delta\tau})\nabla\bar{p}_{\tau+\Delta\tau}]=(1-\bar{C}_{\tau+\Delta\tau})(\phi_f-\phi_{\tau+\Delta\tau}). \tag{2.88}$$

2.2.2 Derivation of the Finite Element Equations of the Problem

Although the finite element method has been broadly used for solving many different types of scientific and engineering problems, the finite element equations related to the chemical dissolution-front propagation problem need to be given blow.

To derive the finite element equations of the problem, three unknown variables involved in the finite difference equations [i.e. Eqs. (2.86)–(2.88)] are defined as follows:

$$U_1 = \Delta\phi_{\tau+\Delta\tau}, \quad U_2 = \bar{C}_{\tau+\Delta\tau}, \quad U_3 = \bar{p}_{\tau+\Delta\tau}. \tag{2.89}$$

By using these new definitions, Eqs. (2.86)–(2.88) can be written in the following forms:

$$f_{U1}U_1 = f_{C1}, \tag{2.90}$$

$$f_{U2}U_2 - \psi^*(\phi_{\tau+\Delta\tau})(\nabla\bar{p}_{\tau+\Delta\tau}\cdot\nabla U_2) - \nabla\cdot[D^*(\phi_{\tau+\Delta\tau})\nabla U_2] = f_{C2}, \tag{2.91}$$

$$\nabla\cdot[\psi^*(\phi_{\tau+\Delta\tau})\nabla U_3] = f_{C3}, \tag{2.92}$$

where

$$f_{U1} = f_{U1}(\bar{C}_{\tau+\Delta\tau}) = \frac{\varepsilon}{\Delta\tau} + (1-\bar{C}_{\tau+\Delta\tau}), \tag{2.93}$$

$$f_{C1} = f_{C1}(\bar{C}_{\tau+\Delta\tau}, \phi_\tau) = (\phi_f - \phi_\tau)(1-\bar{C}_{\tau+\Delta\tau}), \tag{2.94}$$

$$f_{U2} = f_{U2}(\phi_{\tau+\Delta\tau}) = \frac{\varepsilon}{\Delta\tau}\phi_{\tau+\Delta\tau} + \frac{1}{\varepsilon}(\phi_f - \phi_{\tau+\Delta\tau}), \tag{2.95}$$

$$f_{C2} = f_{C2}(\phi_{\tau+\Delta\tau}, \bar{C}_\tau) = \frac{\varepsilon}{\Delta\tau}\phi_{\tau+\Delta\tau}\bar{C}_\tau + \frac{1}{\varepsilon}(\phi_f - \phi_{\tau+\Delta\tau}), \tag{2.96}$$

$$f_{C3} = f_{C3}(\phi_{\tau+\Delta\tau}, \bar{C}_{\tau+\Delta\tau}) = (1-\bar{C}_{\tau+\Delta\tau})(\phi_f - \phi_{\tau+\Delta\tau}). \tag{2.97}$$

Based on the finite element method, the distribution of the above-mentioned three unknown variables in a finite element can be described as follows:

$$U_1^e = [N]\{\Delta_1\}^e, \tag{2.98}$$

$$U_2^e = [N]\{\Delta_2\}^e, \tag{2.99}$$

$$U_3^e = [N]\{\Delta_3\}^e, \tag{2.100}$$

where U_1^e, U_2^e and U_3^e are the distribution fields of the three unknown variables within the finite element; $\{\Delta_1\}^e$, $\{\Delta_2\}^e$ and $\{\Delta_3\}^e$ are the corresponding nodal vectors of the element; $[N]$ is the shape function matrix of the element.

If the finite element under consideration has Q nodes, then the following expressions exist for this element:

$$(\{\Delta_1\}^e)^T = \{\, U_{11} \quad U_{12} \quad \ldots \quad U_{1Q} \,\}, \tag{2.101}$$

$$(\{\Delta_2\}^e)^T = \{\, U_{21} \quad U_{22} \quad \ldots \quad U_{2Q} \,\}, \tag{2.102}$$

$$(\{\Delta_3\}^e)^T = \{\, U_{31} \quad U_{32} \quad \ldots \quad U_{3Q} \,\}, \tag{2.103}$$

$$[N] = [\, N_1 \quad N_2 \quad \ldots \quad N_Q \,], \tag{2.104}$$

where N_i ($i = 1, 2, \ldots, Q$) is the shape function of node i; U_{1i}, U_{2i} and U_{3i} ($i = 1, 2, \ldots, Q$) are the nodal values of the unknown variables for the finite element under consideration.

Using the Galerkin weighted-residual method, Eqs. (2.90)–(2.92) can be rewritten, at the element level, as follows:

$$\left(\iint_A [N]^T f_{U1}[N]\,dA\right)\{\Delta_1\}^e = \iint_A [N]^T f_{C1}\,dA, \tag{2.105}$$

$$\begin{aligned}\left(\iint_A [N]^T f_{U2}[N]dA\right)\{\Delta_2\}^e - \left(\iint_A \psi^*(\phi_{\tau+\Delta\tau})[N]^T(\nabla\bar{p}_{\tau+\Delta\tau}\cdot\nabla[N])dA\right)\{\Delta_2\}^e \\ - \left(\iint_A [N]^T\nabla\cdot(D^*(\phi_{\tau+\Delta\tau})\nabla[N])\,dA\right)\{\Delta_2\}^e = \iint_A [N]^T f_{C2}\,dA,\end{aligned} \tag{2.106}$$

$$\left(\iint_A [N]^T\nabla\cdot\left(\psi^*(\phi_{\tau+\Delta\tau})\nabla[N]\right)dA\right)\{\Delta_3\}^e = \iint_A [N]^T f_{C3}\,dA, \tag{2.107}$$

where A is the area of the element.

Note that the following expressions exist mathematically:

$$\begin{aligned}\left(\iint_A [N]^T\nabla\cdot(D^*(\phi_{\tau+\Delta\tau})\nabla[N])dA\right)\{\Delta_2\}^e = \int_S [N]^T D^*(\phi_{\tau+\Delta\tau})\nabla([N]\{\Delta_2\}^e)dS \\ - \left(\iint_A \nabla[N]^T\cdot(D^*(\phi_{\tau+\Delta\tau})\nabla[N])dA\right)\{\Delta_2\}^e,\end{aligned} \tag{2.108}$$

$$\left(\iint_A [N]^T \nabla \cdot \left(\psi^*(\phi_{\tau+\Delta\tau})\nabla[N]\right) dA\right)\{\Delta_3\}^e = \int_S [N]^T \psi^*(\phi_{\tau+\Delta\tau})\nabla([N]\{\Delta_3\}^e) dS - \left(\iint_A \nabla[N]^T \cdot \left(\psi^*(\phi_{\tau+\Delta\tau})\nabla[N]\right) dA\right)\{\Delta_3\}^e, \tag{2.109}$$

where S is the length of the element boundary.

Substituting Eqs. (2.108) and (2.109) into Eqs. (2.106) and (2.107) yields the following expressions:

$$\begin{aligned}&\left(\iint_A [N]^T f_{U2}[N] dA\right)\{\Delta_2\}^e - \left(\iint_A \psi^*(\phi_{\tau+\Delta\tau})[N]^T(\nabla \bar{p}_{\tau+\Delta\tau} \cdot \nabla[N]) dA\right)\{\Delta_2\}^e \\ &+ \left(\iint_A \nabla[N]^T \cdot (D^*(\phi_{\tau+\Delta\tau})\nabla[N]) dA\right)\{\Delta_2\}^e \\ &= \iint_A [N]^T f_{C2} dA + \int_S [N]^T D^*(\phi_{\tau+\Delta\tau})\nabla([N]\{\Delta_2\}^e) dS,\end{aligned} \tag{2.110}$$

$$\begin{aligned}&\left(\iint_A \nabla[N]^T \cdot \left(\psi^*(\phi_{\tau+\Delta\tau})\nabla[N]\right) dA\right)\{\Delta_3\}^e \\ &= -\iint_A [N]^T f_{C3} dA + \int_S [N]^T \psi^*(\phi_{\tau+\Delta\tau})\nabla([N]\{\Delta_3\}^e) dS.\end{aligned} \tag{2.111}$$

Consideration of Eqs. (2.105), (2.110) and (2.111) leads to the discretized equations of the finite element as follows:

$$[M_1]^e\{\Delta_1\}^e = \{P_1\}^e, \tag{2.112}$$

$$([M_2]^e - [H]^e + [K_1]^e)\{\Delta_2\}^e = \{P_2\}^e, \tag{2.113}$$

$$[K_2]^e\{\Delta_3\}^e = \{P_3\}^e, \tag{2.114}$$

where $[M_1]^e$, $[M_2]^e$, $[H]^e$, $[K_1]^e$ and $[K_2]^e$ are the property matrices of the finite element; $\{P_1\}^e$, $\{P_2\}^e$ and $\{P_3\}^e$ are the "load" vectors of the finite element.

These matrices and vectors can be expressed as follows:

$$[M_1]^e = \iint_A [N]^T f_{U1}[N]\, dA, \tag{2.115}$$

$$[M_2]^e = \iint_A [N]^T f_{U2}[N] dA, \tag{2.116}$$

$$[H]^e = \iint_A \psi^*(\phi_{\tau+\Delta\tau})[N]^T(\nabla \bar{p}_{\tau+\Delta\tau} \cdot \nabla[N])dA, \tag{2.117}$$

$$[K_1]^e = \iint_A \nabla[N]^T \cdot (D^*(\phi_{\tau+\Delta\tau})\nabla[N])dA, \tag{2.118}$$

$$[K_2]^e = \iint_A \nabla[N]^T \cdot (f_{U3b}\nabla[N])dA, \tag{2.119}$$

$$\{P_1\}^e = \iint_A [N]^T f_{C1} dA, \tag{2.120}$$

$$\begin{aligned}\{P_2\}^e &= \iint_A [N]^T f_{C2} dA + \int_S [N]^T D^*(\phi_{\tau+\Delta\tau})\nabla([N]\{\Delta_2\}^e)dS \\ &= \iint_A [N]^T f_{C2} dA + \int_S [N]^T D^*(\phi_{\tau+\Delta\tau})\nabla(\bar{C}_{\tau+\Delta\tau})^e dS,\end{aligned} \tag{2.121}$$

$$\begin{aligned}\{P_3\}^e &= -\iint_A [N]^T f_{C3} dA + \int_S [N]^T \psi^*(\phi_{\tau+\Delta\tau})\nabla([N]\{\Delta_3\}^e)dS \\ &= -\iint_A [N]^T f_{C3} dA + \int_S [N]^T \psi^*(\phi_{\tau+\Delta\tau})\nabla(\bar{p}_{\tau+\Delta\tau})^e dS,\end{aligned} \tag{2.122}$$

where $\nabla(\bar{C}_{\tau+\Delta\tau})^e$ and $\nabla(\bar{p}_{\tau+\Delta\tau})^e$ are the dimensionless chemical-species concentration-gradient and pore-fluid pressure-gradient at the boundary, S, of the finite element.

Assembling the property matrices and vectors of all the elements in a system yields the following discretized governing equations of the system:

$$[M_1]\{\Delta_1\} = \{P_1\}, \tag{2.123}$$

$$([M_2] - [H] + [K_1])\{\Delta_2\} = \{P_2\}, \tag{2.124}$$

$$[K_2]\{\Delta_3\} = \{P_3\}, \tag{2.125}$$

where $[M_1]$, $[M_2]$, $[M_3]$, $[H]$, $[K_1]$ and $[K_2]$ are the global property matrices of the system; $\{P_1\}$, $\{P_2\}$ and $\{P_3\}$ are the global "load" vectors of the system; $\{\Delta_1\}$, $\{\Delta_2\}$ and $\{\Delta_3\}$ are the corresponding global vectors of the system.

Clearly, Eqs. (2.123), (2.124) and (2.125) can be solved separately and sequentially for the porosity, dimensionless concentration and dimensionless pore-fluid pressure at the current time-step. Note that when Eq. (2.123) is solved using the finite element method, the dimensionless concentration at the current time-step is not known. Similarly, when Eq. (2.124) is solved using the finite element method, the dimensionless pore-fluid pressure at the current time-step remains unknown. This

indicates that these three equations are fully coupled so that an iteration scheme needs to be used to solve them sequentially. At the first iteration step, the dimensionless concentration at the previous time-step is used as a reasonable guess of the dimensionless concentration at the current time-step when Eq. (2.123) is solved for the porosity. In a similar way, the dimensionless pore-fluid pressure at the previous time-step is used as a reasonable guess for the current time-step when Eq. (2.124) is solved for the dimensionless concentration. The resulting approximate porosity and dimensionless concentration can be used when Eq. (2.125) is solved for the dimensionless pore-fluid pressure. At the second iteration step, the same procedure as used in the first iteration step is followed, so that the following convergence criterion can be established after the second iteration step.

$$E = Max\left(\sqrt{\sum_{i=1}^{N_\phi}(\phi_{i,\tau+\Delta\tau}^{k}-\phi_{i,\tau+\Delta\tau}^{k-1})^2},\sqrt{\sum_{i=1}^{N_{\bar{C}}}(\bar{C}_{i,\tau+\Delta\tau}^{k}-\bar{C}_{i,\tau+\Delta\tau}^{k-1})^2},\sqrt{\sum_{i=1}^{N_{\bar{p}}}(\bar{p}_{i,\tau+\Delta\tau}^{k}-\bar{p}_{i,\tau+\Delta\tau}^{k-1})^2}\right)<\bar{E}, \tag{2.126}$$

where E and $\bar{E}$ are the maximum error at the k-th iteration step and the allowable error limit; N_ϕ, $N_{\bar{C}}$ and $N_{\bar{p}}$ are the total numbers of the degrees-of-freedom for the porosity, dimensionless concentration and dimensionless pore-fluid pressure respectively; k is the index number at the current iteration step and $k-1$ is the index number at the previous iteration step; $\phi_{i,\tau+\Delta\tau}^{k}$, $\bar{C}_{i,\tau+\Delta\tau}^{k}$ and $\bar{p}_{i,\tau+\Delta\tau}^{k}$ are the porosity, dimensionless concentration and dimensionless pore-fluid pressure of node i at both the current time-step and the current iteration step; $\phi_{i,\tau+\Delta\tau}^{k-1}$, $\bar{C}_{i,\tau+\Delta\tau}^{k-1}$ and $\bar{p}_{i,\tau+\Delta\tau}^{k-1}$ are the porosity, dimensionless concentration and dimensionless pore-fluid pressure of node i at the current time-step but at the previous iteration step. It is noted that $k \geq 2$ in Eq. (2.126).

The convergence criterion is checked after the second iteration step. If the convergence criterion is not met, then the iteration is repeated at the current time-step. Otherwise, the convergence solution is obtained at the current time-step and the solution procedure goes to the next time-step until the final time-step is reached.

2.3 Verification of the Proposed Numerical Algorithm for Simulating the Evolution of Chemical Dissolution Fronts

The main and ultimate purpose of a numerical simulation is to provide numerical solutions for practical problems in a real world. These practical problems are impossible and impractical to solve analytically. Since numerical methods are the basic foundation of a numerical simulation, only an approximate solution can be obtained from a computational model, which is the discretized description of a continuum mathematical model. Due to inevitable round-off errors in computation

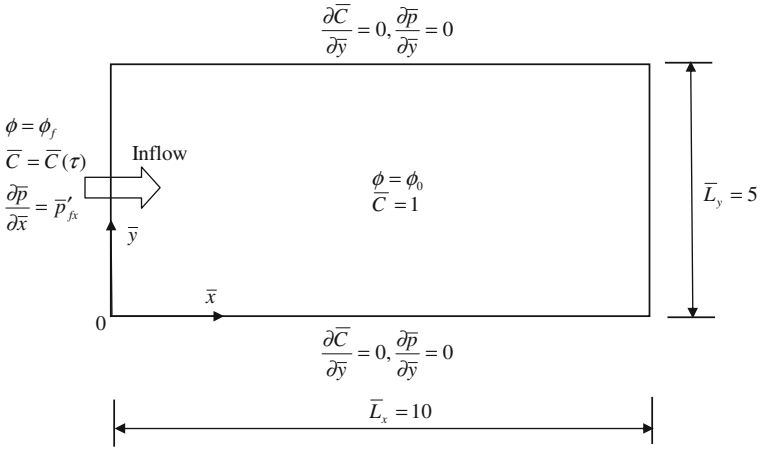

Fig. 2.1 Geometry and boundary conditions of the chemical dissolution problem

and discretized errors in temporal and spatial variables, it is necessary to verify the proposed numerical procedure so that meaningful numerical results can be obtained from a discretized computational model. For this reason, a benchmark problem, for which the analytical solutions are available, is considered in this subsection.

Figure 2.1 shows the geometry and boundary conditions of the coupled problem between porosity, pore-fluid pressure and reactive chemical-species transport within a fluid-saturated porous medium. For this benchmark problem, the dimensionless-pressure gradient (i.e. $\bar{p}'_{fx} = -1$) is applied on the left boundary, implying that there is a horizontal throughflow from the left to the right of the computational model. In this case, the Zhao number of the reactive transport system is unity. The dimensionless height and width of the computational model are 5 and 10 respectively. Except for the left boundary, the initial porosity of the porous medium is 0.1, while the initial dimensionless-concentration is one within the computational domain. The final porosity after depletion of the soluble mineral is 0.2. This final porosity is applied on the left boundary as a boundary condition of the computational domain. The permeability of the porous medium is calculated using the Carman-Kozeny formula, which has the power of 3 in the power law. The diffusivity of chemical species is calculated using the power law, which has the power of 2. Both the top and the bottom boundaries are assumed to be impermeable for the pore-fluid and chemical species. The mineral dissolution ratio of the chemical dissolution system is assumed to be 0.01, while the dimensionless time-step length is set to be 0.005 in the computation. Since the computational domain of the benchmark problem is of finite size, a time-dependent-dimensionless-concentration boundary condition [i.e. $\bar{C}(\tau) = \exp(\bar{p}'_{fx}\bar{v}_{front}\tau)$] needs to be applied on the left boundary so that the numerical solutions can be compared with

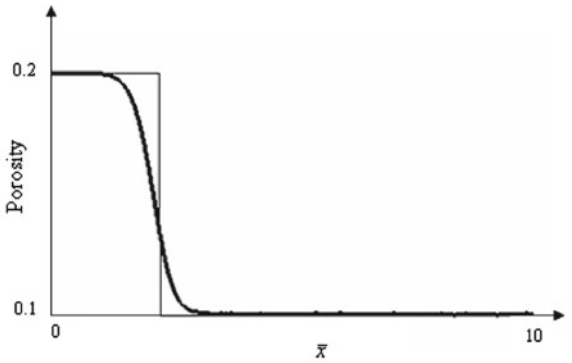

($\tau = 0.25$)

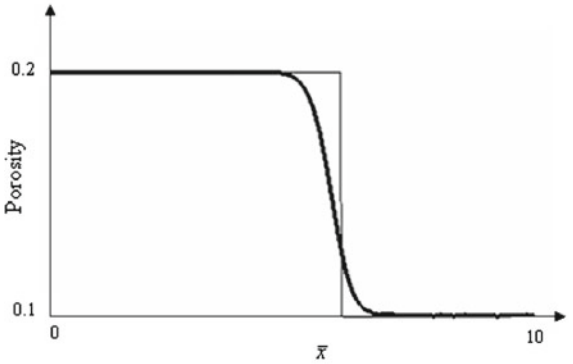

($\tau = 0.625$)

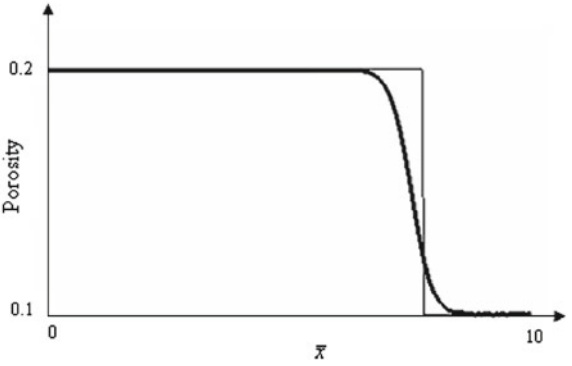

($\tau = 0.8$)

Fig. 2.2 Comparison of numerical solutions with analytical ones at different time instants (porosity): the *thick line* shows the numerical results, while the *thin line* shows the corresponding analytical solutions

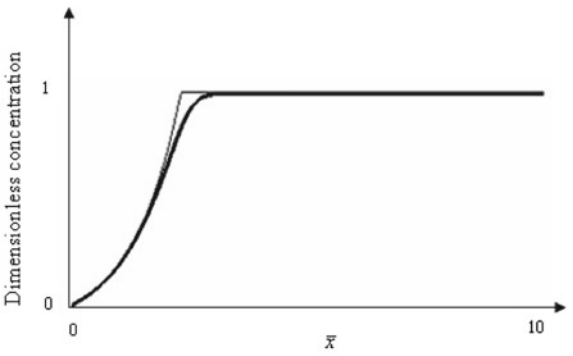

($\tau = 0.25$)

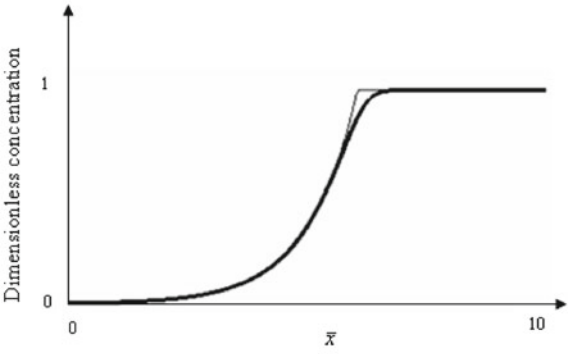

($\tau = 0.625$)

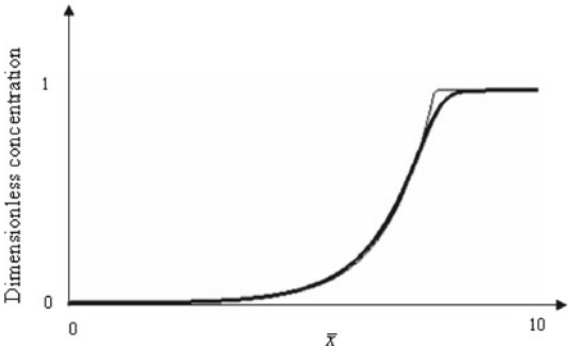

($\tau = 0.8$)

Fig. 2.3 Comparison of numerical solutions with analytical ones at different time instants (dimensionless concentration): the *thick line* shows the numerical results, while the *thin line* shows the corresponding analytical solutions

the analytical solutions derived in the previous section. Using the above-mentioned parameters, the critical Zhao number of the system is approximately equal to 1.77. Since the Zhao number of the system is greater than its critical value, the

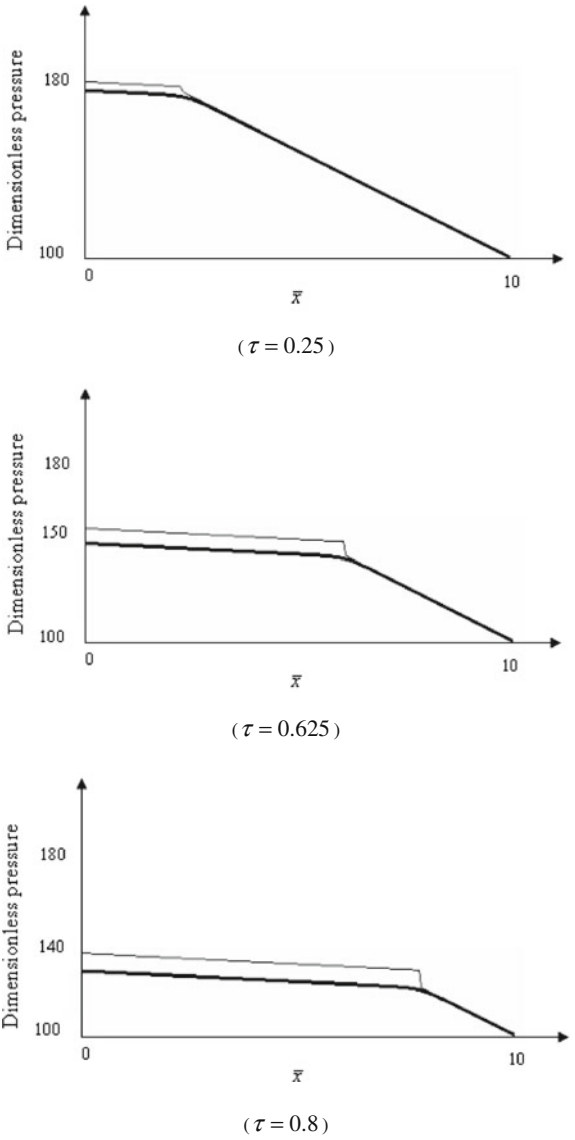

Fig. 2.4 Comparison of numerical solutions with analytical ones at different time instants (dimensionless pore-fluid pressure): the *thick line* shows the numerical results, while the *thin line* shows the corresponding analytical solutions

coupled system considered in this subsection is sub-critical so that a planar dissolution front remains planar during its propagation within the system. The dimensionless speed of the dissolution front propagation is equal to 10, which is determined using Eq. (2.52). To simulate appropriately the propagation of the

dissolution front, the whole computational domain is simulated by 19701 four-node rectangular elements of 20,000 nodal points in total.

Figures 2.2, 2.3, and 2.4 show the comparison of numerical solutions with analytical ones for the porosity, dimensionless concentration and dimensionless pore-fluid pressure distributions within the computational domain at three different time instants. In these figures, the thick line shows the numerical results, while the thin line shows the corresponding analytical solutions, which can be determined from Eqs. (2.50) and (2.51) with the boundary condition of $\bar{p}(\bar{L}_x, \tau) = 100$ at the right boundary of the computational model. The resulting analytical solutions are expressed as follows:

$$\bar{C}(\bar{x}, \tau) = 1, \quad \phi(\bar{x}, \tau) = \phi_0 \quad (\bar{x} > \bar{v}_{front}\tau), \tag{2.127}$$

$$\bar{p}(\bar{x}, \tau) = -\bar{p}'_{0x}(\bar{L}_x - \bar{x}) + 100 \quad (\bar{x} > \bar{v}_{front}\tau), \tag{2.128}$$

$$\bar{C}(\bar{x}, \tau) = \exp[-\bar{p}'_{fx}(\bar{x} - \bar{v}_{front}\tau)], \quad \phi(\bar{x}, \tau) = \phi_f \quad (\bar{x} \le \bar{v}_{front}\tau), \tag{2.129}$$

$$\bar{p}(\bar{x}, \tau) = \bar{p}'_{fx}(\bar{x} - \bar{v}_{front}\tau) - \bar{p}'_{0x}(\bar{L}_x - \bar{v}_{front}\tau) + 100 \quad (\bar{x} \le \bar{v}_{front}\tau)\,. \tag{2.130}$$

From these results, it can be observed that the numerical solutions agree very well with the analytical solutions, indicating that the proposed numerical procedure is capable of simulating the planar dissolution-front propagation within the fluid-saturated porous medium. As expected, the porosity propagation front is the sharpest one among the three propagation fronts, namely a porosity propagation front, a dimensionless-concentration propagation front and a dimensionless-pressure propagation front, in the computational model. Clearly, the dimensionless-pressure propagation front has the widest bandwidth, implying that it is the least sharp front in the computational model. Although there are some smoothing effects on the numerically-simulated propagation fronts as a result of numerical dispersion, the propagation speed of the numerically-simulated propagation front is in good coincidence with that of the analytically-predicted propagation front. For this benchmark problem, the overall accuracy of the numerical results is indicated by the dimensionless pore-fluid pressure. The maximum relative error of the numerically-simulated dimensionless pore-fluid pressure is 2.2, 4.6 and 5.8 % for dimensionless times of 0.25, 0.625 and 0.8 respectively. If both a small mesh size and a small time-step length are used, then the maximum relative error can be further reduced in the numerical simulation. This quantitatively demonstrates that the proposed numerical procedure can produce accurate numerical solutions for the planar dissolution-front propagation problem within a fluid-saturated porous medium.

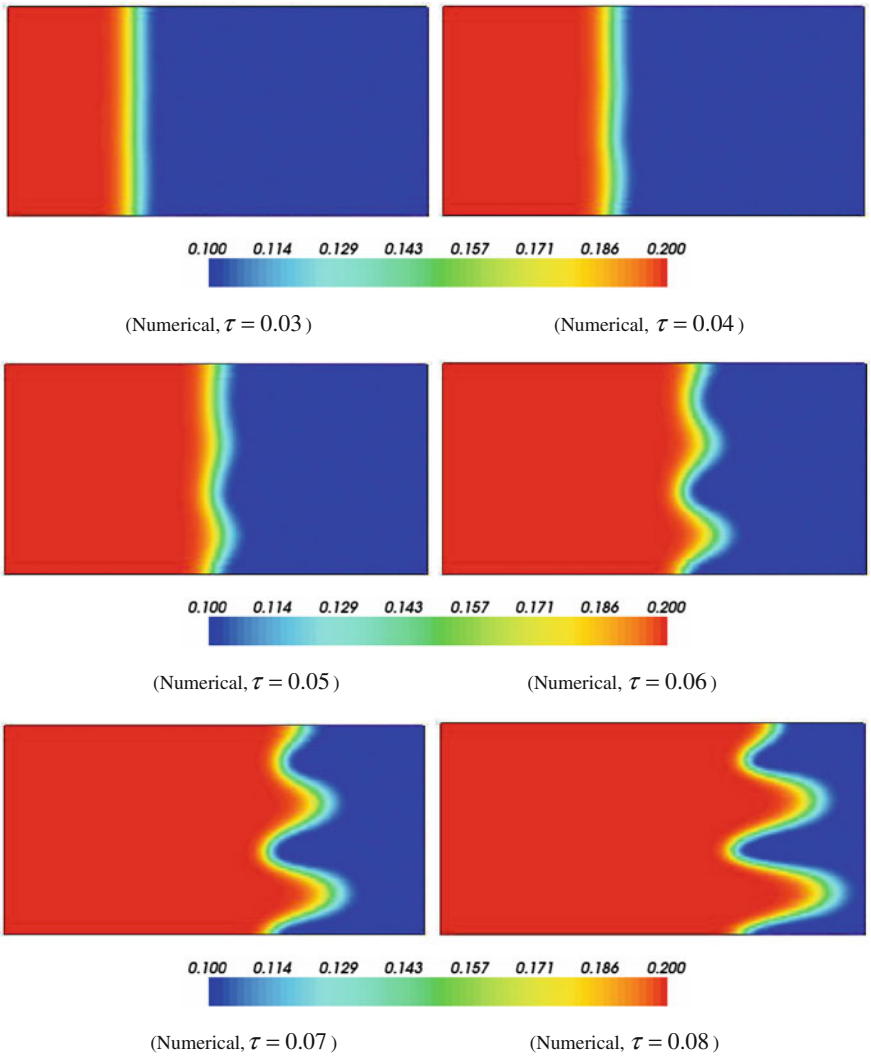

Fig. 2.5 Porosity distributions due to morphological evolution of the chemical dissolution front in the fluid-saturated porous medium

2.4 An Application Example for Simulating the Morphological Evolution of Chemical Dissolution Fronts

In this section, the proposed numerical procedure is used to simulate the morphological evolution of a chemical dissolution front in a supercritical system. For this purpose, a dimensionless-pressure gradient (i.e. $\bar{p}'_{fx} = -10$) is applied on the

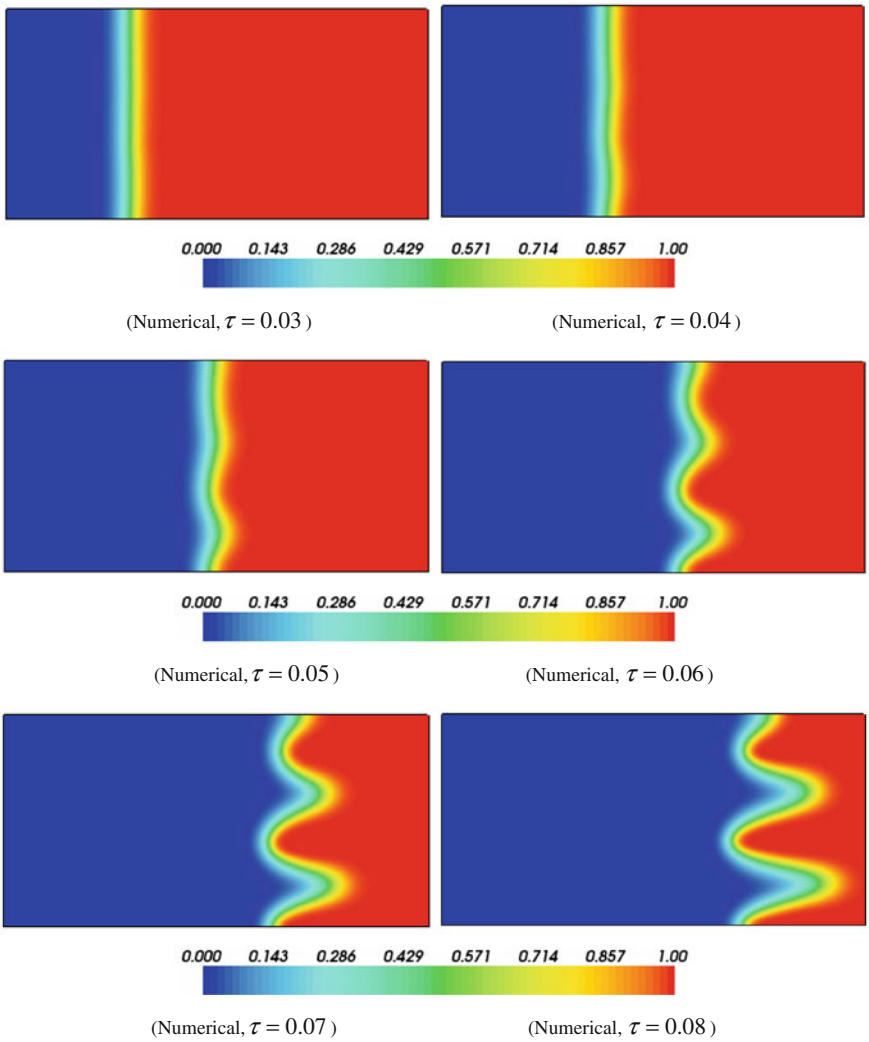

Fig. 2.6 Dimensionless concentration distributions due to morphological evolution of the chemical dissolution front in the fluid-saturated porous medium

left boundary of the computational domain so that the dimensionless speed of the dissolution front propagation is equal to 100. This means that the dissolution front propagates much faster than it does within the system considered in the previous section. Due to this change, the mineral dissolution ratio of the chemical dissolution system is assumed to be 0.001, while the dimensionless time-step length is also assumed to be 0.001 in the computation. The Zhao number of the system is increased to 10, which is greater than the critical Zhao number (i.e. approximately

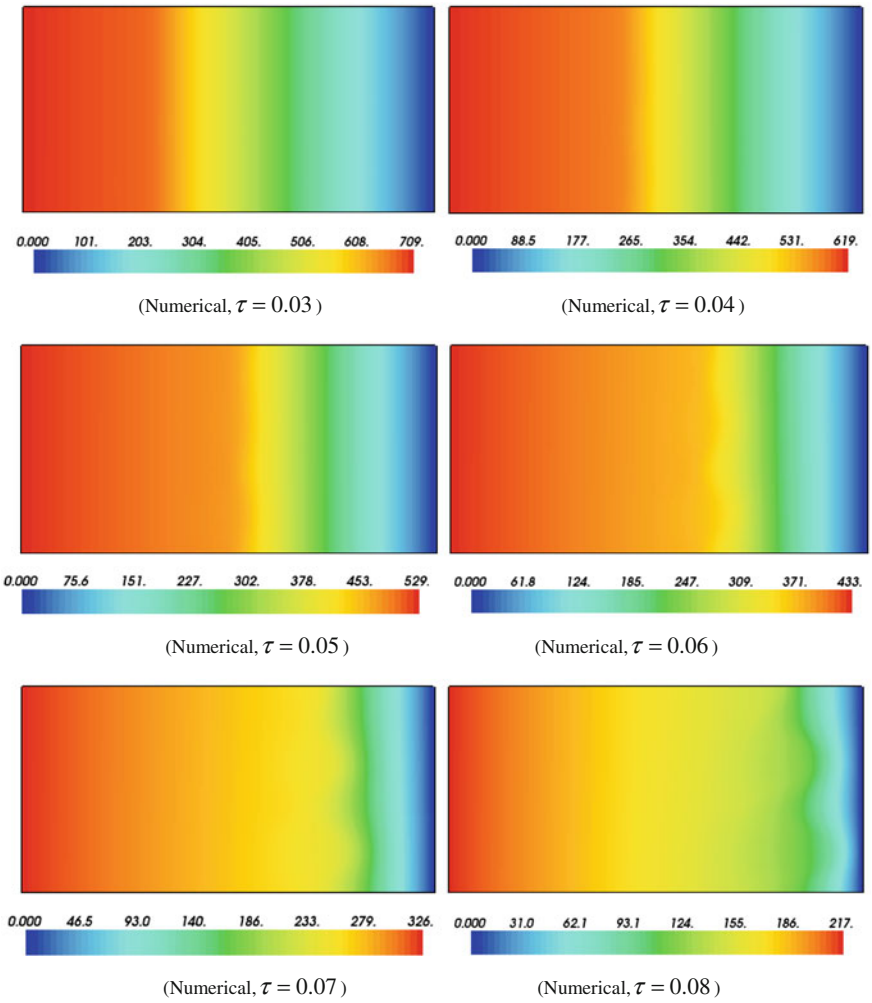

Fig. 2.7 Dimensionless pore-fluid pressure distributions due to morphological evolution of the chemical dissolution front in the fluid-saturated porous medium

1.77) of the system. The values of other parameters are exactly the same as those used in the previous section. Since the Zhao number of the system is smaller than its critical value, the coupled system considered in this section is supercritical so that a planar dissolution front evolves into a complicated morphology during its propagation within the system. In order to simulate the instability of the chemical dissolution front, a small perturbation of 1 % initial porosity is randomly added to the initial porosity field in the computational domain.

Figure 2.5 shows the porosity distributions due to the morphological evolution of the chemical dissolution front in the fluid-saturated porous medium, while

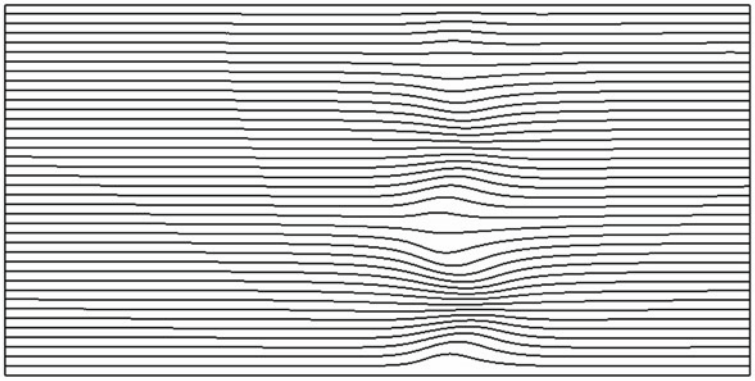

($\tau = 0.06$)

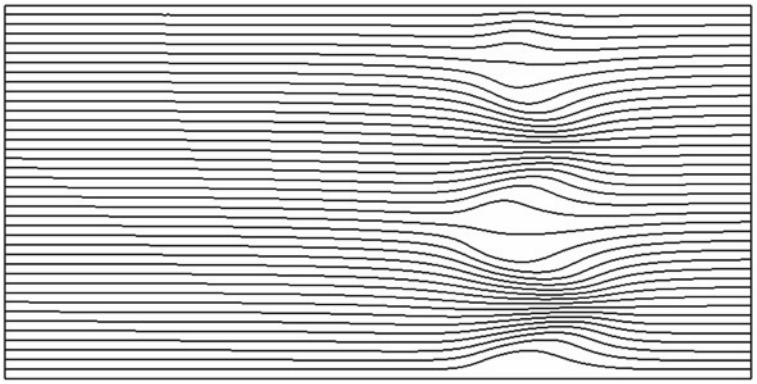

($\tau = 0.07$)

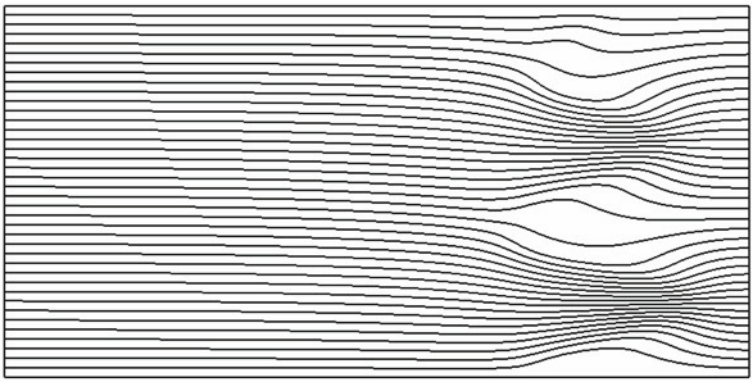

($\tau = 0.08$)

Fig. 2.8 Streamline distributions due to morphological evolution of the chemical dissolution front in the fluid-saturated porous medium

Fig. 2.6 shows the dimensionless concentration distributions due to the morphological evolution of the chemical dissolution front within the computational domain. It is observed that for the values of the dimensionless time greater than 0.03, the initial planar dissolution-front gradually changes into an irregular one. With a further increase of the dimensionless time, the amplitude of the resulting irregular dissolution-front increases significantly, indicating that the chemical dissolution front is morphologically unstable during its propagation within the computational model. Although both the porosity and the dimensionless concentration have a similar propagation front, the distribution of their maximum values along the dissolution front is clearly different. The peak value of the porosity is in good correspondence with the trough value of the dimensionless concentration due to the chemical dissolution in the system. This demonstrates that the proposed numerical procedure is capable of simulating the morphological instability of the chemical dissolution front in a fluid-saturated porous medium in the case of the coupled system being supercritical.

It is interesting to investigate how the dimensionless pore-fluid pressure and pore-fluid flow evolve with time during the propagation of the unstable dissolution front in the computational model. Figure 2.7 shows the dimensionless pore-fluid pressure distributions during the morphological evolution of the chemical dissolution front. It is noted that although the dimensionless pore-fluid pressure is continuous, there exists a clear transition for the dimensionless pressure-gradient distribution in the computational model. This phenomenon can be clearly seen at the late stages of the numerical simulation such as when the dimensionless time is equal to 0.06 and 0.07. The fluid-flow pattern evolution during the propagation of the unstable dissolution front is exhibited by the streamline evolution in the computational model. Figure 2.8 shows the streamline distributions during the morphological evolution of the chemical dissolution front within the coupled system between porosity, pore-fluid pressure and reactive chemical-species transport. Due to the growth of the amplitude of the irregular dissolution front, pore-fluid flow focusing takes place in the peak range of the porosity, which can be observed from the streamline density (in Fig. 2.8). It is noted that the width of the flow focusing zone is closely associated with the peak and trough values of the irregular dissolution front in the computational model. Since both the porosity generation and the pore-fluid flow focusing play an important role in ore body formation and mineralization, the proposed numerical procedure can provide a useful tool for simulating the related physical and chemical processes associated with the generation of giant ore deposits within the upper crust of the Earth.

References

Bear J (1972) Dynamics of fluids in porous media. American Elsevier, New York

Chadam J, Hoff D, Merino E, Ortoleva P, Sen A (1986) Reactive infiltration instabilities. IMA J Appl Math 36:207–221

Chadam J, Ortoleva P, Sen A (1988) A weekly nonlinear stability analysis of the reactive infiltration interface. IMA J Appl Math 48:1362–1378

Chen JS, Liu CW (2002) Numerical simulation of the evolution of aquifer porosity and species concentrations during reactive transport. Comput Geosci 28:485–499

Detournay E, Cheng AHD (1993) Fundamentals of poroelasticity. In: Hudson JA, Fairhurst C (eds) Comprehensive rock engineering, Vol. 2: analysis and design methods. Pergamon Press, New York

Gow P, Upton P, Zhao C, Hill K (2002) Copper-gold mineralization in the New Guinea: numerical modeling of collision, fluid flow and intrusion-related hydrothermal systems. Aust J Earth Sci 49:753–771

Lewis RW, Schrefler BA (1998) The finite element method in the static and dynamic deformation and consolidation of porous media. Wiley, New York

Nield DA, Bejan A (1992) Convection in porous media. Springer, New York

Ormond A, Ortoleva P (2000) Numerical modeling of reaction-induced cavities in a porous rock. J Geophys Res 105:16737–16747

Ortoleva P, Chadam J, Merino E, Sen A (1987) Geochemical self-organization II: the reactive-infiltration instability. Am J Sci 287:1008–1040

Phillips OM (1991) Flow and reactions in permeable rocks. Cambridge University Press, Cambridge

Raffensperger JP, Garven G (1995) The formation of unconformity-type uranium ore deposits: coupled hydrochemical modelling. Am J Sci 295:639–696

Schafer D, Schafer W, Kinzelbach W (1998a) Simulation of reactive processes related to biodegradation in aquifers: 1. Structure of the three-dimensional reactive transport model. J Contam Hydrol 31:167–186

Schafer D, Schafer W, Kinzelbach W (1998b) Simulation of reactive processes related to biodegradation in aquifers: 2. Model application to a column study on organic carbon degradation. J Contam Hydrol 31:187–209

Schaubs P, Zhao C (2002) Numerical modelling of gold-deposit formation in the Bendigo-Ballarat zone, Victoria. Aust J Earth Sci 49:1077–1096

Scheidegger AE (1974) The physics of flow through porous media. University of Toronto Press, Toronto

Steefel CI, Lasaga AC (1990) Evolution of dissolution patterns: permeability change due to coupled flow and reaction. In: Melchior DC, Basset RL (eds.) Chemical modeling in aqueous systems II, American Chemistry Society Symposium Series, vol. 416, pp. 213–225

Steefel CI, Lasaga AC (1994) A coupled model for transport of multiple chemical species and kinetic precipitation/dissolution reactions with application to reactive flow in single phase hydrothermal systems. Am J Sci 294:529–592

Turcotte DL, Schubert G (1982) Geodynamics: applications of continuum physics to geological problems. Wiley, New York

Xu TF, Samper J, Ayora C, Manzano M, Custodio E (1999) Modelling of non-isothermal multi-component reactive transport in field scale porous media flow systems. J Hydrol 214:144–164

Xu TF, Apps JA, Pruess K (2004) Numerical simulation of CO2 disposal by mineral trapping in deep aquifers. Appl Geochem 19:917–936

Yeh GT, Tripathi VS (1991) A model for simulating transport of reactive multispecies components: model development and demonstration. Water Resour Res 27:3075–3094

Zhao C, Xu TP, Valliappan S (1994) Numerical modelling of mass transport problems in porous media: a review. Comput Struct 53:849–860

Zhao C, Hobbs BE, Mühlhaus HB (1998) Finite element modelling of temperature gradient driven rock alteration and mineralization in porous rock masses. Comput Methods Appl Mech Eng 165:175–187

Zhao C, Hobbs BE, Mühlhaus HB, Ord A (1999) Finite element analysis of flow patterns near geological lenses in hydrodynamic and hydrothermal systems. Geophys J Int 138:146–158

Zhao C, Hobbs BE, Walshe JL, Mühlhaus HB, Ord A (2001a) Finite element modeling of fluid-rock interaction problems in pore-fluid saturated hydrothermal/sedimentary basins. Comput Methods Appl Mech Eng 190:2277–2293

Zhao C, Hobbs BE, Mühlhaus HB, Ord A (2001b) Finite element modelling of rock alteration and metamorphic process in hydrothermal systems. Commun Numer Methods Eng 17:833–843

Zhao C, Lin G, Hobbs BE, Ord A, Wang Y, Mühlhaus HB (2003) Effects of hot intrusions on pore-fluid flow and heat transfer in fluid-saturated rocks. Comput Methods Appl Mech Eng 192:2007–2030

Zhao C, Hobbs BE, Ord A, Peng S, Mühlhaus HB, Liu L (2005) Numerical modeling of chemical effects of magma solidification problems in porous rocks. Int J Numer Meth Eng 64:709–728

Zhao C, Hobbs BE, Ord A, Hornby P (2006a) Chemical reaction patterns due to fluids mixing and focusing around faults in fluid-saturated porous rocks. J Geochem Explor 89:470–473

Zhao C, Hobbs BE, Hornby P, Ord A, Peng S (2006b) Numerical modelling of fluids mixing, heat transfer and non-equilibrium redox chemical reactions in fluid-saturated porous rocks. Int J Numer Meth Eng 66:1061–1078

Zhao C, Hobbs BE, Ord A, Hornby P, Peng S, Liu L (2007) Mineral precipitation associated with vertical fault zones: the interaction of solute advection, diffusion and chemical kinetics. Geofluids 7:3–18

Zhao C, Hobbs BE, Hornby P, Ord A, Peng S, Liu L (2008a) Theoretical and numerical analyses of chemical-dissolution front instability in fluid-saturated porous rocks. Int J Numer Anal Meth Geomech 32:1107–1130

Zhao C, Hobbs BE, Ord A, Hornby P, Peng S (2008b) Effect of reactive surface areas associated with different particle shapes on chemical-dissolution front instability in fluid-saturated porous rocks. Transp Porous Media 73:75–94

Zhao C, Hobbs BE, Ord A, Hornby P, Mühlhaus HB, Peng S (2008c) Theoretical and numerical analyses of pore-fluid-flow focused heat transfer around geological faults and large cracks. Comput Geotech 35:357–371

Zhao C, Hobbs BE, Ord A, Peng S (2010) Effects of mineral dissolution ratios on chemical-dissolution front instability in fluid-saturated porous media. Transp Porous Media 82:317–335

Zienkiewicz OC (1977) The finite element method. McGraw-Hill, London

http://www.springer.com/978-3-319-08460-2

Physical and Chemical Dissolution Front Instability in Porous Media
Theoretical Analyses and Computational Simulations
Zhao, C.
2014, XVIII, 354 p. 93 illus., 68 illus. in color., Hardcover
ISBN: 978-3-319-08460-2